Equivalent Shock-Associated Noise Source Reconstruction of Screeching Underexpanded Unheated Round Jets

D.J. Tan[*] and D. Honnery[†],

Monash University, Clayton, Victoria, 3800, Australia

A. Kalyan[‡], V. Gryazev[§], and S.A. Karabasov[¶],

Queen Mary University of London, Mile End Road, London E1 4NS, United Kingdom

D. Edgington-Mitchell[‖]

Monash University, Clayton, Victoria, 3800, Australia

This paper investigates the broadband shock-associated noise (BBSAN) radiated from supersonic jets at the root source level. The sources are modelled according to an acoustic analogy. The acoustic analogy model is informed by high spatial resolution 2D-2C particle image velocimetry (PIV) data and solutions to the Reynolds-Averaged Navier-Stokes (RANS) equations for the reconstruction of the equivalent BBSAN sources. The measurements are of screeching underexpanded jets issuing from a purely converging nozzle at ideally expanded Mach numbers of 1.45 and 1.59. The jet conditions are simulated using a RANS solver with a $k - \omega$ shear stress transport turbulence model. The RANS scales are modelled using formulations of a two-time scale model based on the turbulence dissipation and large eddy convection time. The large eddy convection based scale is recommended as a replacement for the standard turbulence dissipation scale in low-order BBSAN models. The equivalent BBSAN sources are reconstructed from the PIV measurements and RANS solutions at the peak Strouhal number. The equivalent BBSAN sources extracted from the PIV and RANS data are shown to have favourable agreement.

American Institute of Aeronautics and Astronautics

Nomenclature

α Mixed-scale model parameter

$\boldsymbol{\eta}$ Displacement vector, (ξ, η, ζ)

$\boldsymbol{x}$ Observer location

$\boldsymbol{y}$ Source location, (x, y, z)

ϵ Dissipation rate

γ Ratio of specific heat

$\hat{\tau}$ Functional time scale

$\hat{L}$ Functional length scale

κ Wave number

κ_1 Axial wavenumber

Λ Upper limit of integral length scale

Ω Specific dissipation rate

ω Angular frequency

$\overline{V_i}$ Mean velocity

π Non-dimensional pressure, $1/\gamma \ln(p/p_\infty)$

ψ Stream function

Re Reynolds number

ρ Density

τ Time separation

τ_s Integral time scale

θ Observer polar angle relative to the downstream jet axis

[*]Ph.D. Student, Laboratory for Turbulence Research in Aerospace and Combustion, Department of Mechanical and Aerospace Engineering, dominic.tan@monash.edu, and AIAA Member

[†]Professor, Laboratory for Turbulence in Aerospace and Combustion, Department of Mechanical and Aerospace Engineering, damon.honnery@monash.edu, and AIAA Member

[‡]Ph.D Student, School of Engineering and Material Sciences, a.kalyan@qmul.ac.uk, and AIAA member

[§]Ph.D Student, School of Engineering and Material Sciences, v.gryazev@qmul.ac.uk, and AIAA member

[¶]Reader in Computational Modelling, School of Engineering and Material Sciences, s.karabasov@qmul.ac.uk, and AIAA Senior Member

[‖]Senior Lecturer, Laboratory for Turbulence Research in Aerospace and Combustion, Department of Mechanical and Aerospace Engineering, daniel.mitchell@monash.edu, and AIAA Member

American Institute of Aeronautics and Astronautics

θ_i Dilatation source term

$\tilde{p}_s$ Axial Fourier transform of shock pressure

a Speed of sound

C_p Specific heat at constant pressure

c_τ Time scale coefficient

c_L Length scale coefficient

D Nozzle diameter

$f(\tau_1, \tau_2)$ Non-dimensional time scale function

f_i^a Turbulence/acoustic source term

f_i^v Turbulence/shock source term

k Turbulence kinetic energy

L Integral length scale

L_1 Length of domain in the streamwise direction

M Mach number

p Pressure

p_s Shock pressure

R^v Velocity correlation function

r^v Velocity correlation coefficients

$S(\mathbf{x}, \omega)$ Power spectral density of far-field pressure

$s(\mathbf{y}, \omega)$ Equivalent BBSAN source

t Time

v_i Velocity fluctuations

Subscripts

0 Stagnation condition

∞ Free-stream condition

c Convective component

e Exit condition

j Ideally expanded condition

American Institute of Aeronautics and Astronautics

s	Shock fluctuations
x	Observer direction

Superscripts

(phi)	Direction of integration
$\prime$	Random fluctuating component
a	Acoustic component
c	Coherent velocity component
v	Velocity component

I.   Introduction

Shock-associated noise is a component of the noise radiated by imperfectly expanded supersonic jets. These jets have a plume with a potential core that consists of a quasi-periodic shock cell structure. The shock cell structure results from the imperfect expansion at the jet exit. The shock cell structure is characterised by a series of compression and expansion waves that reflect off the high-speed side of the jet shear layer to form a shock tip. The shock tips can interact with large-scale turbulence in the shear layer to generate the shock-associated noise. The shock-associated noise consists of discrete (screech) and broadband (BBSAN) components that primarily radiate in the sideline directions relative to the jet. The screech mechanism is characterised by a self-reinforcing acoustic resonance phenomenon [1] that is produced through interactions between periodic high-energy large-scale turbulence fluctuations in the shear layer and the shock tips. Acoustic-turbulence interactions between the screech tones and turbulence can amplify the broadband noise [2]. The broadband shock-associated noise is generated by weak interactions between random large-scale turbulence fluctuations and the shock tips [3–7].

The early jet noise prediction methodologies for BBSAN heavily relied on experimental databases [8]. The semi-empirical nature of the early BBSAN prediction methods restricts their applicability to conditions similar to those contained in the database. Harper-Bourne and Fisher's [8] pioneering prediction scheme used a least-squares analysis of an extensive

measurement database, with the BBSAN sources represented by an array of monopoles located at the intersection between the shear layer and the shock tips. The shock cells were assumed to be equally spaced, which results in harmonic peaks of BBSAN with approximately equal intensity. These features are not observed in experiments [6] as peak turbulence fluctuations occur in the regions directly upstream of the oblique compression waves of the shock cells.

Tam [5] presented a prediction scheme for the BBSAN radiated by over- and under-expanded jets issuing from converging and converging-diverging axisymmetric nozzles. The initial development of the model considered the random large-scale turbulence, which is modelled as a random superposition of instability waves [9]. The shock cell structure was then modelled using a multiple-scales expansion to account for the growth rate of the shear layer, the dissipative effects of the turbulence on the shock cells, and adduced heating effects [10]. These developments were consolidated into a stochastic theory for shock-associated noise [5, 11]. Tam's stochastic theory [5] describes the shock-associated noise process as one produced by the coherent scattering of the large turbulence structures as they pass through the shock cells. A similarity argument is used to establish the source model, but breaks down for higher Strouhal number computations such that overall sound pressure levels cannot be determined by integrating over all frequencies. The model predicts both the near and far-field spectra of BBSAN for axisymmetric jets at moderately off-design conditions with favourable agreement to experiments. However, further comparisons to experiments by Morris and Miller [12] indicate that there are inconsistencies between over- and underexpanded conditions at large observer angles to the jet axis.

Limitations associated with the early prediction schemes were overcome through the use of an acoustic analogy [13]. Acoustic analogies principally consist of a rearrangement of the compressible Navier-Stokes equations into linear and non-linear parts that describe the propagation and generation of the sound, respectively. The non-linear part is representative of the equivalent noise sources, which are assumed to be known, or can

American Institute of Aeronautics and Astronautics

at least be approximated. The propagation of the sound can be handled using integral methods [14] (Kirchhoff integral [15], Ffowcs-Williams Hawking [16] or linearised Euler equations [17, 18]) so that the problem is reduced to finding a representation of the equivalent noise sources.

A BBSAN acoustic analogy with a linear wave propagation operator was developed by Morris and Miller [12]. Morris and Miller's model builds on Tam's analysis [5] to overcome some of the empiricism associated with previous models [5, 8] by relying on solutions to the Reynolds-Averaged Navier-Stokes (RANS) equations with a two-equation turbulence model. The equivalent acoustic sources are analytically approximated by a statistical model that links the mean flow to the dominant noise mechanisms. The statistical model separates the spatial and temporal characteristics, which are theoretically defined by integral time and length scales, respectively. The integral scales are usually modelled based on the local mean turbulence statistics. The model coefficients are determined by matching predictions to far-field acoustic measurements for a single jet condition and observer location [12]. The coefficients are then held constant for subsequent predictions. The validity of some of the models and assumptions used in the development of statistical RANS-based BBSAN acoustic analogies are assessed in the current work.

Reliable noise predictions depend strongly on the accuracy of the RANS solutions and the statistical model describing the equivalent acoustic sources. Morris and Zaman [19] measured the streamwise components of the velocity autocovariance tensor and amplitudes of some transverse components using hot wires. Further experiments by Morris and Zaman [20] completed the transverse measurements and length scales. These experiments provide well-resolved temporal information of some of the two-point turbulence statistics that need to be modelled in acoustic analogy prediction schemes. High spatial-resolution measurements acquired at low frequency can be achieved with particle image velocimetry (PIV) techniques. Spatially-resolved PIV measurements typically yield statistically independent velocity fields. Statistical analysis of the velocity fields can provide the mean and RMS velocities, and spatial correlations that can support models for BBSAN. Tan et

al. [21] analysed the correlations of high spatial resolution 2D-2C PIV measurements of screeching unheated round jets. Functional scales based on the mean turbulence statistics were later linearly fit to the integral length scales [22]. The proportionality coefficients of the random turbulence length scales were shown to be insensitive to operating condition for screeching jets at ideally expanded Mach numbers of 1.45 and 1.59. Savarese et al. [23] presented spatial BBSAN source maps, which were determined from the space-frequency coherence of simultaneous near-field pressure and velocity measurements. The spatial source maps indicate that the source activity is localised on the high-speed frontier of the jet with an axial distribution of localised spots, most intense just upstream of the compression wave focus. The location of regions of BBSAN production relative to the shock reflection point is supported by results presented by Kalyan and Karabasov [24].

This paper builds on the analysis of Tan et al. [21, 22] to model the origins of BBSAN in the same jets at the root source level. Screeching unheated round jets issuing from a purely converging nozzle at ideally expanded Mach numbers M_j of 1.45 and 1.59 are considered. The acoustic analogy is informed by high spatial resolution 2D-2C PIV measurements and RANS solutions with a $k - \omega$ turbulence closure model. Temporal information required to evaluate the integral time scales is not available from the PIV measurements, so noise predictions are note considered. The PIV measurements contain periodic high-energy, large-scale fluctuations associated with the screech mechanism, which are filtered *a posteriori* [21]. The filtered fluctuations are used to evaluate the turbulence statistics, which have been analysed by Tan et al. [22]. The analysis yielded proportionality coefficients that are used to model the RANS scales in the current study. The equivalent BBSAN sources are then reconstructed from the PIV measurements and RANS solutions at the peak BBSAN frequency ($Sr = 1$). The source reconstruction is used to provide an assessment on the accuracy of characteristic low-order turbulence scale models for modelling the equivalent BBSAN sources in axisymmetric jets. To the authors' knowledge, this is the first time the equivalent BBSAN sources have been reconstructed from PIV measurements.

American Institute of Aeronautics and Astronautics

The paper is laid out as follows. Sec. II describes the theory for modelling BBSAN with an acoustic analogy. The acoustic analogy is informed by PIV measurements and RANS simulations of supersonic jets. The jets considered are described in Sec. IV, which includes a description of the experimental data that is relevant to the BBSAN source analysis. The RANS solutions used to model the equivalent BBSAN sources are presented in Sec. V. A description of the flow-field simulations is provided with details on the post-processing of the numerical data. The RANS solutions are shown to have excellent agreement with the PIV measurements. The equivalent BBSAN sources are then presented in Sec. VI.

II.   Acoustic Analogy Theory for BBSAN

As the BBSAN acoustic analogy model of Morris and Miller [12] provides the theoretical base for the work presented herein, this section will provide a recapitulation of the model framework. The flow variables are decomposed into: a steady mean flow (overbar); perturbations associated with the shock cell structure (s); fluctuations associated with the turbulence (t); and the acoustic fluctuations generated by the interaction of the turbulence and the shock cell structure ($\prime$). For high Reynolds (Re) number cold jets, the viscous and heat conduction effects may be ignored. By considering only the leading-order fluctuations, the governing system of equations in terms of pressure and velocity are

$$\frac{\partial \pi'}{\partial t} + \bar{v}_j \frac{\partial \pi'}{\partial x_j} + \frac{\partial v_i'}{\partial x_i} = \theta_i \tag{1}$$

$$\frac{\partial v_i'}{\partial t} + \bar{v}_j \frac{\partial v_i'}{\partial x_j} + v_j' \frac{\partial \bar{v}_i}{\partial x_j} + \bar{a}^2 \frac{\partial \pi'}{\partial x_i} = f_i^{\mathrm{v}} + f_i^{\mathrm{a}} \tag{2}$$

and

$$\pi = \frac{1}{\gamma} \ln\left(\frac{p}{p_\infty}\right) \tag{3}$$

where v_i is the velocity, and p and p_∞ denote the static and ambient pressures, respectively. The dilatation, turbulence/shock, and turbulence/acoustic source terms are represented by θ_i, f_i^{v}, and f_i^{a}, respectively. The turbulence/acoustic source term f_i^{a} is dependent on

temperature fluctuations. Simulations suggest that f_i^{a} is not important for cold jets [25] so is not considered. The dilatation rate source term is expected to scale similarly to f_i^{v}, which is described by

$$f_i^{\mathrm{v}} = -v_{sj}\frac{\partial v_{ti}}{\partial x_j} - v_{tj}\frac{\partial v_{si}}{\partial x_j} \tag{4}$$

This source term scales based on characteristic turbulent velocity fluctuations v_{t}, characteristic length scales L, and the strength of the shock cells p_{s} such that $f_i^{\mathrm{v}} \sim p_{\mathrm{s}}v_{\mathrm{t}}/(\rho_\infty a_\infty L)$ [12] where

$$p_s(\boldsymbol{y}) = p(\boldsymbol{y}) - p_\infty(\boldsymbol{y}) \tag{5}$$

In this model, the second-order correlations of f_i^{v} represent the BBSAN sources, which are modelled using the Proudman form of the cross-correlation function for isotropic turbulence [26]. The correlations are defined as

$$R^v_{f^{\mathrm{v}}_x f^{\mathrm{v}}_x}(\boldsymbol{y},\boldsymbol{\eta},\tau) = \langle f^{\mathrm{v}}_x(\boldsymbol{y},t)\,f^{\mathrm{v}}_x(\boldsymbol{y}+\boldsymbol{\eta},t+\tau)\rangle \tag{6}$$

where f_x^v denotes the component of f_i^v in the direction of the observer. Thus, for an observer in the sideline direction, the transverse ($x = 2$) component is important. The equivalent BBSAN source term may then be expressed in terms of the product of the second-order velocity correlations and the shock pressure such that

$$R^{\mathrm{v}}_{f^{\mathrm{v}}_x f^{\mathrm{v}}_x}(\boldsymbol{y},\boldsymbol{\eta},\tau) = \frac{1}{\rho_\infty^2 a_\infty^2 L^2}p_s(\boldsymbol{y})\,p_s(\boldsymbol{y}+\boldsymbol{\eta})\,R^{\mathrm{v}}(\boldsymbol{y},\boldsymbol{\eta},\tau) \tag{7}$$

where $\boldsymbol{\eta} = (\xi,\eta,\zeta)$, $\tau = t + \tau_1$, and $R^{\mathrm{v}}(\boldsymbol{y},\boldsymbol{\eta},\tau)$ is the spatio-temporal velocity correlation function. In the sideline directions, propagation effects due to the mean flow are expected to be small, so that the power spectral density (PSD) of the far-field pressure can be estimated using a free-space Green's function approximation. The PSD may thus be

expressed as

$$S(\boldsymbol{x}, \omega) = \frac{\omega^2}{16\pi^2 a_\infty^4 |\boldsymbol{x}|^2} \int_{-\infty}^{\infty} \cdots \int_{-\infty}^{\infty} \frac{1}{L^{(1)^2}} p_s(\boldsymbol{y}) p_s(\boldsymbol{y} + \boldsymbol{\eta}) R^v(\boldsymbol{y}, \boldsymbol{\eta}, \tau)$$

$$\times e^{i\omega(\tau - \boldsymbol{x} \cdot \boldsymbol{\eta}/(xa_\infty))} \; d\tau \; d\boldsymbol{\eta} \; d\boldsymbol{y} \quad (8)$$

where ω is the angular frequency, a_∞ is the ambient speed of sound, $|\boldsymbol{x}|$ is the distance to the observer, and $L^{(1)}$ is a characteristic streamwise length scale. The free-space approximation can be replaced with a vector Green's function when temperature effects become significant [27].

A. Equivalent BBSAN Source

An advantage of the acoustic analogy is that the noise sources can be spatially localised at different frequencies. The spatial locations of the equivalent BBSAN sources are defined by the inner integral of Eq.(8). In the Morris and Miller model, the spatio-temporal velocity correlations $R^v(\boldsymbol{y}, \boldsymbol{\eta}, \tau)$ are modelled by assuming that the time and space variables are separable [28]. The spatio-temporal velocity correlations may then be approximated [12] by

$$R^v(\boldsymbol{y}, \boldsymbol{\eta}, \tau) = R^v(\boldsymbol{y}, 0, 0)\, e^{-|\tau|/\tau_s} e^{-(\xi - \bar{v}_c \tau)^2/L^{(1)^2}} e^{-(\eta^2 + \zeta^2)^2/L^{(2)^2}} \quad (9)$$

where $R^v(\boldsymbol{y}, 0, 0)$ is the auto-covariance of the velocity fluctuations, $\overline{v_c}$ is the convective velocity, and the temporal and spatial characteristics are described by time scales τ_s, and streamwise and cross-stream length scales $L^{(1)}$ and $L^{(2)}$, respectively. The correlation model given by Eq. (9) is an exponential function, so does not capture strong negative correlations that are associated with screech-related fluctuations. The time and length scales are theoretically defined by the shape of the second-order velocity correlation function, or can be modelled by the mean turbulence statistics. The correlation model given by Eq.(9) is used to approximate the equivalent BBSAN sources for a given angular

frequency ω and observer location θ relative to the downstream jet axis by

$$
s\left(\boldsymbol{y}, \omega\right) = \int_{-\infty}^{\infty} \left\{ \frac{R^{\mathrm{v}}\left(\boldsymbol{y}, 0, 0\right) L^{(2)2}}{L^{(1)} \tau_{\mathrm{s}}} p_{\mathrm{s}}\left(\boldsymbol{y}\right) \widetilde{p}_{\mathrm{s}}\left(\kappa_1, y_2, y_3\right) e^{i\kappa_1 y_1} \right.
$$
$$
\left. \times \frac{\omega^2 \tau_{\mathrm{s}}^2 e^{-L^{(1)2}\left(\kappa_1 - \omega \cos \theta / a_\infty\right)^2/4} - \omega^2 L^{(2)2} \sin^2 \theta / \left(4 a_\infty^2\right)}{1 + \left(1 - M_{\mathrm{c}} \cos \theta + \overline{u_{\mathrm{c}}} \kappa_1 / \omega\right)^2 \omega^2 \tau_{\mathrm{s}}^2} \right\} \mathrm{d}\kappa_1 \quad (10)
$$

where the integration over the axial wave number κ_1 results from the application of the axial Fourier transform to one of the shock pressure terms in Eq. (8) [12]. The equivalent BBSAN sources approximated by Eq. (10) represent the jet locations that contribute most to the sound in the sideline direction at a particular frequency. Temperature effects at the source level may be accounted for by evaluating Eq. (10) with the local flow properties instead of the ambient values [27].

B.   Source Calculation

The equivalent BBSAN sources are modelled according to Eq. (10) using the local flow properties. The convective velocity is approximated by the local axial mean velocity along the nozzle lip line of the jet [19, 29]. The time and length scales can be evaluated based on the definitions in Table 2. The correlation scale models are informed by either the scales calculated from PIV measurements or steady RANS solutions. The Fourier transform of the shock pressure $\tilde{p}_{\mathrm{s}}$ is performed on an even function obtained by mirroring the shock pressure p_{s} about the nozzle exit plane. A Hanning window with an energy correction factor of 8/3 is applied to the shock pressure before a discrete Fourier transform. The transformed shock pressure is integrated over the axial wavenumber domain κ_1 using Simpson's rule with the spacing given by $2\pi/L_1$, where L_1 is the axial extent of the domain.

III.   Functional Scales

Accurate noise predictions require that the integral scales are properly defined as they describe the temporal and spatial behaviour of the noise sources. The scales along the

nozzle lip line have been demonstrated to be important for noise source modelling [19]. In the sideline directions, the correlation scales of the transverse velocity fluctuations are needed to model the equivalent BBSAN sources. The source scales are theoretically defined by the integral of the two-point two-time spatio-temporal velocity correlations [30]. A direct calculation of the integral length scales requires both spatially and temporally resolved data. In the absence of spatially and temporally resolved data, the integral scales may instead be modelled via relationships to functional scales. The functional time and length scales, $\hat{\tau}$ and $\hat{L}$, respectively, are formulated as ratios of the mean turbulence statistics with dimensions of time or length [31]. The ratios are usually constructed in terms of mean flow properties that are yielded by RANS solutions with a two-equation turbulence model. Expressing the low-order length scale models as ratios generally enables a representation of the integral scales that can be understood in terms of the local mean turbulence statistics. The simplest low-order integral scale model assumes that the turbulence scales are directly proportional to functional scales.

In the absence of spatially and temporally resolved data, the integral scales may instead be approximated via relationships to functional scales. The functional time and length scales, $\hat{\tau}$ and $\hat{L}$, respectively, are formulated as ratios of the mean turbulence statistics with dimensions of time or length [31]. The time and length scales important for noise source modelling are generally assumed to be directly proportional to the functional scales via fixed coefficients that are valid over a range of jet conditions. For fixed coefficient values, NPR, and total temperature ratio scaling can be accounted for using an equivalent source that depends on the local density, speed of sound, and streamwise velocity components with a vector Green's function to handle refraction effects due to the shear layer [27].

A.   Two-Time-Scale Model

A two-time scale approach for modelling the source scales was implemented by Kalyan and Karabasov [24] to explicitly take into account the dependence of the BBSAN generation mechanism on the strength of the shock cells. The generation mechanism is described

American Institute of Aeronautics and Astronautics

by two random processes with functional time scales $\hat{\tau}_1$ and $\hat{\tau}_2$. These time scales are associated with the random large-scale turbulence, and shock cell effects, respectively. The correlated part of the noise generation mechanism is represented by $\hat{\tau}_2$. The functional time scale $\hat{\tau}_s$ that is dependent on both $\hat{\tau}_1$ and $\hat{\tau}_2$ is modelled according to

$$\hat{\tau}_\text{s} = c_\tau \hat{\tau}_1 \cdot \begin{cases} f(\hat{\tau}_1, \hat{\tau}_2), & \text{if} \quad f(\hat{\tau}_1, \hat{\tau}_2) > 1 \\ 1, & \text{else} \end{cases} \tag{11}$$

where $f(\hat{\tau}_1, \hat{\tau}_2)$ is a non-dimensional power law given by

$$f(\hat{\tau}_1, \hat{\tau}_2) = \left(\frac{\hat{\tau}_1}{\hat{\tau}_2} \right)^\alpha \tag{12}$$

In this relation, α controls the relative contributions of the two time scales with values of 0 or 2 for the BBSAN acoustic analogy model of Morris and Miller model [12], or the mixed-scale model of Kalyan and Karabasov [24], respectively. For the mixed-scale model, in regions where the shocks are weak, the function tends to 1 so that only contributions associated with τ_1 are considered.

Table 1. Functional scales considered for $\hat{\tau}_1$

Model	$\hat{\tau}_1$
Turbulence dissipation	$\dfrac{k}{\epsilon}$
Large eddy convection	$\dfrac{D_\text{j}}{\overline{\overline{v_1}}}$

The time scale, $\hat{\tau}_1$, is approximated using two low-order models in the present study. The models considered are associated with the turbulence dissipation and the large eddy convection time, which are summarised in Table 1. The second time scale τ_2 is inversely proportional to the mean axial velocity gradient for both cases.

The functional streamwise length scales are estimated based on a mean square proce-

American Institute of Aeronautics and Astronautics

Table 2. Definitions of the correlation scales for modelling the equivalent BBSAN sources in the sideline direction

	Time scale	Streamwise length scale	Transverse length scale
Theory [30]:	$\tau_s = \int\limits_0^{\Lambda} r_{22}^v(\boldsymbol{y}, \boldsymbol{\eta} = 0, \tau)\ \mathrm{d}\tau$	$L_{22}^{(1)} = \int\limits_0^{\Lambda} r_{22}^v(\boldsymbol{y}, \xi, \tau = 0)\ \mathrm{d}\xi$	$L_{22}^{(2)} = \int\limits_0^{\Lambda} r_{22}^v(\boldsymbol{y}, \eta, \tau = 0)\ \mathrm{d}\eta$
Two-time-scale model:	$\hat{\tau}_s = c_\tau \hat{\tau}_1 \cdot \begin{cases} f(\hat{\tau}_1, \hat{\tau}_2), & \text{if}\quad f(\hat{\tau}_1, \hat{\tau}_2) > 1 \\ 1, & \text{else} \end{cases}$	$\hat{L}^{(1)} = c_{L^{(1)}}\sqrt{k}\,\hat{\tau}_s$	$\hat{L}^{(2)} = c_{L^{(2)}}\hat{L}^{(1)}$

dure that is applied to the integral length scale. The functional streamwise length scales are estimated based on the mean square velocity and the characteristic time scale $\hat{\tau}_s$. The transverse length scale is determined based on an anisotropy relationship relative to the streamwise length scale. The definitions of the correlation scales that are important for modelling the equivalent BBSAN sources in the sideline direction are given in Table 2. The upper limit of integration is chosen to minimise the low-correlation noise. The proportionality coefficients that relate the models to the integral scales are assumed to be fixed for a range of jet conditions [12, 24, 32].

IV.   LTRAC Supersonic Jets

The BBSAN acoustic analogy theory is applied to high-spatial resolution 2D-2C PIV measurements of screeching cold round jets at ideally expanded Mach numbers of $M_j = 1.45$ and 1.59. The data was acquired in the Laboratory for Turbulence Research in Aerospace and Combustion (LTRAC) Supersonic Jet Facility at Monash University [33,34]. The jets considered radiate screech in the helical C instability mode [33], with a higher intensity when the jet is operated at the $M_j = 1.45$ condition [34]. Additional details on the screech mechanism, internal flow structure, and velocity decomposition of the LTRAC supersonic jet PIV data has been presented in previous work [21, 33, 34]. A summary of the jet conditions and boundary conditions used in the PIV analysis and modelling is

provided in Table 3.

Table 3. Summary of the PIV jet parameters and boundary conditions used for modelling the BBSAN

	M_j	
	1.45	1.59
NPR	3.4	4.2
D_j (mm)	16.02	16.73
Re_j ($\times 10^5$)	8.51	10.6
T_∞ (K)	288	288
T_0 (K)	288	288

A. PIV Measurements

Table 4. Non-dimensional PIV parameters for a multigrid cross-correlation algorithm [35]

Parameter	Value	Non-dimensional value
Total number of vectors	182×1000	—
IW_0	64 pixels	$0.10\ D$
IW_1	16 pixels	$0.025\ D$
Grid spacing	8 pixels	$0.013\ D$
Depth of field	2.4 mm	$0.17\ D$
Light sheet thickness	1.5 mm	$0.1\ D$
Δt	480 ns	—
Field of view	150 mm $\times$ 35 mm	$10\ D \times 2.2\ D$
Maximum resolvable velocity	830 m/s	$2.6\ V_e$
Minimum resolvable velocity	6 m/s	$0.02\ V_e$

The PIV measurements were conducted in the LTRAC Supersonic Jet Facility, which supplies compressed air to the plenum chamber at approximately 288 K. The compressed air is connected directly to the mixing chamber where the free stream and jet is uniformly seeded with oil particles from a Vicount 1300 smoke generator. The ambient free stream pressure and temperature is assumed to be at sea level conditions for both cases. The mix-

American Institute of Aeronautics and Astronautics

ing chamber is connected to the plenum chamber, which contains a honeycomb section and wire mesh screens to condition the flow. The nozzle pressure ratio ($NPR = P_0/P_\infty$) is maintained within 1% via a Fairchild 100 High Flow pressure regulator. The stagnation pressure in the plenum is measured using an RS-461 pressure transducer with an uncertainty of ±0.25% over a range of $0-10$ bar. This translates to an uncertainty of ±0.9 kPa and ±1.1 kPa for NPRs of 3.4 and 4.2, respectively. Compressed air issues from a 15 mm diameter round nozzle with a lip thickness of 5 mm. The nozzle has a short purely converging section so that the flow is sonic at the exit with a velocity of V_e = 310 m/s. A complete description of the facility and the PIV system can be found in previous work [33, 34, 36]. Complications specific to the application of PIV to supersonic flows in this facility have been thoroughly investigated [37].

The PIV measurements yielded 8500 statistically independent velocity fields for each jet condition. The optical arrangement had two orthogonally mounted PCO 4000 cameras, each with a full array size of 4008×2672 pixels. Each camera was fitted with 105 mm Micro Nikkor Nikon lenses set to an aperture of f/5.6. The resulting images have an optical resolution of 23 μm/pixel. A 1.5 mm plane was illuminated by a NewWave Solo PIV Nd:YAG laser at 532 nm wavelength, which was run with an inter-framing time between images of Δt = 480 ns. The calculated velocity fields from the two cameras were stitched together using a convolution with an adaptive Gaussian window [38] that overlapped by 7.5%, which results in an effective field of view of 10 $D \times 2.2$ D.

A multigrid cross-correlation digital particle image velocimetry (MCCDPIV) algorithm [35] with an adaptive interrogation window technique was used. The adaptive interrogation window iteratively reduces an initial window size of IW_0 to a final size of IW_1, which were 64 pixels and 16 pixels, respectively, with a 50% overlap. The maximum resolvable velocity was estimated based on a displacement of 25% of the initial interrogation window size. The minimum resolvable velocity was based on a conservative estimate of the minimum resolvable displacement as 0.1 ± 0.06 pixels (95% confidence level) [35]. A summary of the PIV parameters is presented in Table 4.

Erroneous vectors were identified by a dynamic mean value operator and replaced by interpolation with immediate neighbours. Bias errors are introduced by the discretisation of the flow-field and particle lag effects. The combination of both discretisation and particle lag errors makes it difficult to quantify the uncertainty in the velocity measurements and calculated turbulence statistics.

1. Pressure Reconstruction

The spatial pressure variation p_s is modelled from the PIV measurements by assuming steady isentropic and adiabatic flow. For these flows, the stagnation conditions are conserved along the mean streamlines of the time-invariant mean velocity fields. The mean streamlines are defined by the two-dimensional stream function ψ, which is given by

$$\psi = \int \left(\overline{V}_1 \, dx_2 - \overline{V}_2 \, dx_1 \right) \tag{13}$$

along which the total pressure is conserved. In regions where the streamlines are closed, such as within the potential core, isentropic relations are used to approximate the total pressure ratio by

$$\frac{p}{P_0} = \left(1 + \frac{\gamma - 1}{2} M^2 \right)^{-\gamma/(\gamma-1)} \tag{14}$$

where P_0 is the stagnation pressure and M is the local Mach number. In the potential core, the stagnation pressure is approximated from the NPR. Additional post-processing, which is not considered in this study, are required in cases where there is a strong Mach disk [39]. The local Mach number is calculated according to

$$M = \sqrt{\gamma R T} \tag{15}$$

American Institute of Aeronautics and Astronautics

where T is the local static temperature defined by

$$T = T_0 - \frac{\overline{V}^2}{2C_p} \tag{16}$$

and T_0 is the stagnation temperature. Eq. (16) holds only if the ambient and jet total temperatures are equal. When the ambient and total temperatures differ, the Crocco-Busemann relation given by

$$T = -\frac{1}{2}\overline{V}^2 + C_1\overline{V} + C_2 \tag{17}$$

should be used, where

$$C_1 = \frac{1 - (T_2/T_1)}{\gamma - 1} + \frac{M_a}{2} \tag{18}$$

$$C_2 = \frac{T_2/T_1}{\gamma - 1} + \frac{M_a^2}{2} - M_a C_1 \tag{19}$$

In the jet shear layer, the pressure is determined by spatially integrating the time-invariant mean pressure gradient. Following van Oudheusden etal [40], the density term is replaced with pressure and temperature using the ideal gas law and the adiabatic assumption such that the mean pressure gradient may be expressed as

$$\frac{-\nabla p}{p} = \frac{\gamma M_\infty^2}{V_\infty^2 + \frac{\gamma - 1}{2}M_\infty^2\left(V_\infty^2 - \overline{V}x^2\right)} \cdot (\mathbf{V} \cdot \nabla)\,\mathbf{V} \tag{20}$$

Eq. (20) is integrated using a fourth-order finite-difference scheme with boundary conditions imposed at the edge of the potential core and the outer shear layer. The outer edge is set by the regions where $M = 0.01$.

2. Flow Velocity Decomposition

The fluctuating velocity fluctuations in screeching jets contain random and coherent components. These components are assumed to be superimposed on a mean flow such that the total velocity can be expressed as

$$V_i(y, t) = \overline{V}_i(y) + v_i'(y, t) + v_i^c(y, t) \tag{21}$$

with the mean, random, and coherent components denoted by $\overline{V}_i$, v_i', and v_i^c, respectively. The total velocity fluctuations v_i is the sum of the random and coherent components. The mean is steady, hence, radiates no sound, while the coherent and random components are considered to consist of the fluctuations that contribute only to the screech and broadband noise, respectively. The BBSAN is studied in terms of the velocity fluctuations by filtering the coherent component associated with the screech tones. The coherent velocity fluctuations contain the high-energy large-scale periodic motion associated with the helical C instability screech mode, which is dominant for both jet conditions considered.

The coherent velocity fluctuations are determined using a snapshot POD method as outlined in Tan et al. [21]. The POD-based triple decomposition involves identifying the POD modes that sufficiently capture the periodic large-scale coherent motion present in the jet. Tan et al. identified through a spectral analysis that the periodic motion is well captured by the leading pair of POD modes for the LTRAC jet cases considered in this study. The velocity fluctuations contributing to the helical C instability mode are filtered by subtracting the coherent velocity fluctuations from Eq. (21), and thus their ability to generate noise. A shock capturing technique was not considered for the discontinuous behaviour across shocked regions in the potential core [41] as the fluctuations in the shear layer are more relevant in the consideration of BBSAN.

The generation of BBSAN includes contributions from all coherent structures, as well as all scales of turbulence. However, these contributions are not necessarily periodic in nature. The POD analysis does not remove all structures at those scales, but only those

that are periodic within the spatial domain. Thus, the reconstructed random velocity fluctuations consist of all structures and scales except the periodic large-scale coherent structures attributed to the screech tones, while the non-periodic structures at this wavelength remain. The fluctuations without the periodic self-forcing component can be used as input to an acoustic analogy. Tone-induced turbulence amplification from the presence of screech [42] is expected to be retained as the effects have been shown to manifest in the smaller scales of turbulence [43].

The POD-based method was originally demonstrated using the PIV measurements used in this study. The study [21] showed that the second-order integral length scales exhibited a similar scaling with the shear layer thickness to sub- and supersonic non-screeching jet experiments [44, 45] when the coherent velocity fluctuations are filtered. It should be noted that the absolute values differed. The reliability of the POD-based method was assessed through a sensitivity analysis of the second-order integral length scales [21]. The sensitivity analysis examined several grid resolutions and signal-to-noise ratios (SNR) for the POD analysis and integral length scale calculations. The error relative to calculations using the full resolution data is less than 1% when there are at least 3000 vector fields and a SNR greater than 500, while the error is approximately 1.5% when the PIV mesh is down-sampled to 146×800 vectors. The sensitivity of the POD analysis and length scale calculations to the sample size and rate was found to fall within the ranges predicted in similar studies [21, 46–48]. The amplification of the random velocity fluctuations due to the presence of screech is expected to be on the order of the uncertainty in the POD analysis [21].

3. Turbulence Scale Contributions

The contribution of the different turbulence scales defined in the two time-scale model is given by the non-dimensional function $f(\hat{\tau}_1, \hat{\tau}_2)$. Streamwise distributions of $f(\hat{\tau}_1, \hat{\tau}_2)$ are reproduced in Fig. 1. The contribution of $\hat{\tau}_1$ to the time scale associated with the generation of BBSAN dominates for the LTRAC jets [22]. In the framework of the mixed-
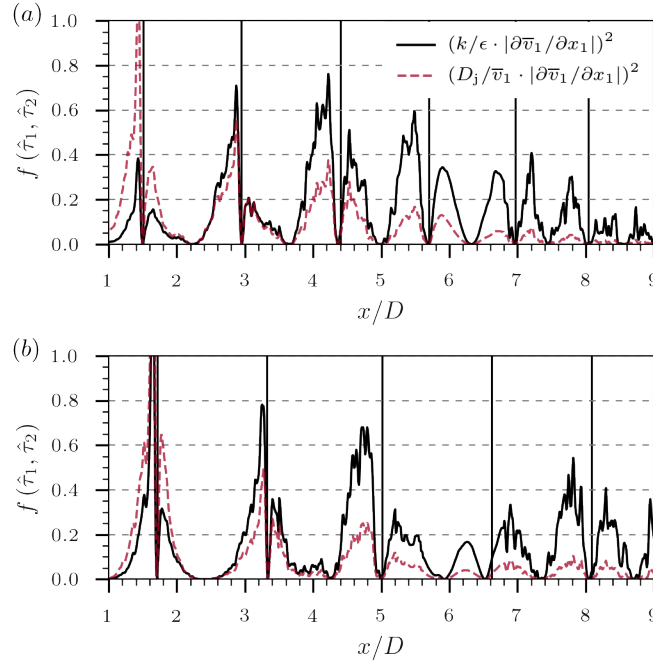
American Institute of Aeronautics and Astronautics

Figure 1. Streamwise distributions of the non-dimensional function $f(\tau_1, \tau_2)$ for M_j of (a) 1.45 and (b) 1.59. From [22].

scale model [24], this suggests that contributions to the time scale from the random turbulence dominates over the shock cell effects for the LTRAC jets. Importantly, the same conclusion follows from either using the standard turbulence dissipation scale or the large eddy convection scale model.

B. BBSAN Source Variables

The variables that define the equivalent BBSAN sources in the sideline direction are determined from the PIV measurements. The jet turbulence is assumed to be statistically axisymmetric such that the mean turbulence kinetic energy k and dissipation rate ϵ may be estimated by imposing axisymmetric mean flow assumptions where

$$
\begin{aligned}
\langle v_2' v_2' \rangle &\approx \langle v_3' v_3' \rangle \\
\left\langle \frac{\partial v_2'}{\partial x_j} \frac{\partial v_2'}{\partial x_j} \right\rangle &\approx \left\langle \frac{\partial v_3'}{\partial x_j} \frac{\partial v_3'}{\partial x_j} \right\rangle \\
\left\langle \frac{\partial v_i'}{\partial x_2} \frac{\partial v_i'}{\partial x_2} \right\rangle &\approx \left\langle \frac{\partial v_i'}{\partial x_3} \frac{\partial v_i'}{\partial x_3} \right\rangle
\end{aligned}
\tag{22}
$$

The mean turbulence kinetic energy and dissipation rate are then given by

$$k = \frac{1}{2} \left\langle v_i' v_i' \right\rangle \quad \text{and} \quad \epsilon = v \left\langle \frac{\partial v_i'}{\partial x_k} \frac{\partial v_i'}{\partial x_k} \right\rangle \tag{23}$$

where v is the kinematic viscosity of air at normal conditions. An improved estimation of the kinematic viscosity might consider the density determined from the ideal gas law with the thermodynamic temperature and pressure outlined in Sec. 1, and Sutherland's law for modelling viscosity. The accuracy in the dissipation rate calculation is determined by the resolution of the PIV measurements [49]. Bias errors introduced in the calculation of the velocity gradients are expected to increase the uncertainty in the functional scale based on the turbulence dissipation.

The functional PIV length and time scales are evaluated based on the models in Table 2. The proportionality coefficient for the time scales is specified as 1. The length scale proportionality coefficients are based on a linear fit between the functional scales and the integral length scales along the nozzle lip line [22]. The integral length scales were evaluated with an upper limit of integration defined by

$$r^v \left(\boldsymbol{x}, \boldsymbol{\eta} = \Lambda, \tau = 0 \right) = 0.1 \tag{24}$$

where Λ is the axial separation distance corresponding to a correlation of 0.1. A cut-off criteria of 0.1 was used to avoid the low-correlation noise and contributions from negative correlations that are observed in screeching jets. An additional time scale is determined by rearranging the streamwise length scale model equation given in Table 2 such that

$$\hat{\tau}_s \sim L^{(1)} / \sqrt{k} \tag{25}$$

in order to reduce the number of assumptions used. Eq. (25) is used with the integral length scales to provide a higher-order model for the noise sources based on the PIV.
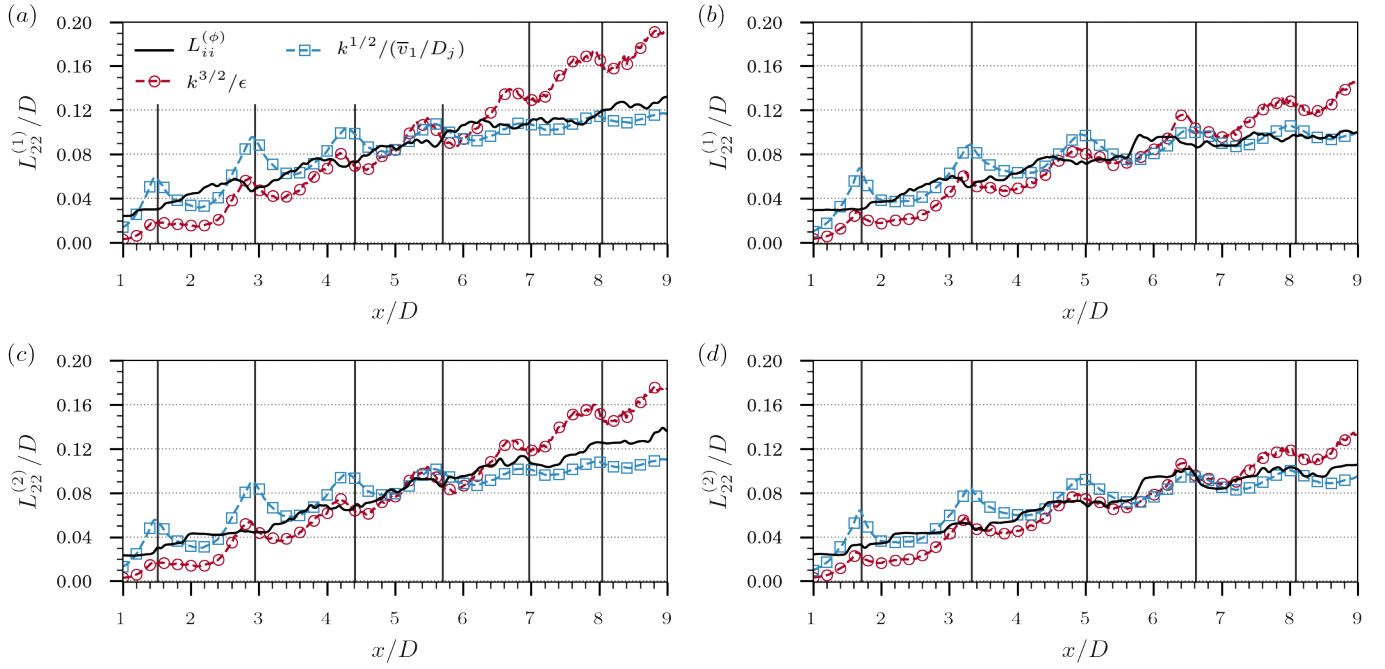
American Institute of Aeronautics and Astronautics

1. Length Scales

Figure 2. Lip-line distributions of the streamwise second-order length scales for M_j of **(a, c)** 1.45 and **(b, d)** 1.59. From [22].

Table 5. Proportionality coefficients including the RMS dispersion error measured with PIV [22]

	M_j		
	1.45	1.59	Mean
$L_{22}^{(\phi)} = c_{L_{22}^{(\phi)}} k^{3/2}/\epsilon$			
$c_{L_{22}^{(1)}}$	0.29±0.06	0.27±0.02	0.28
$c_{L_{22}^{(2)}}$	0.28±0.05	0.26±0.05	0.27
$L_{22}^{(\phi)} = c_{L_{22}^{(\phi)}} k^{1/2}/(\bar{v}_1/D_j)$			
$c_{L_{22}^{(1)}}$	0.44±0.07	0.42±0.06	0.43
$c_{L_{22}^{(2)}}$	0.42±0.08	0.41±0.06	0.42

The equivalent BBSAN sources that radiate noise in the sideline directions depend on the length scales of the random transverse velocity fluctuations. The streamwise and

transverse length scales are evaluated from the transverse velocity fluctuations measured with PIV using the coefficients in Table 2. Distributions of these length scales have been presented in previous work [21, 22]. The streamwise length scales of the transverse velocity fluctuations that are of relevance to modelling the BBSAN in the sideline direction are reproduced in Fig. 2 for $1 < x/D < 9$, with the axial locations of the shock reflection points indicated by the vertical lines. Over this domain, the mean square error is less than 3% for the turbulence dissipation and large eddy convection time correlation models. The mean square error is consistent for both jet conditions considered.

The proportionality coefficients for the second-order length scales of the random transverse velocity fluctuations that minimise the RMS dispersion error between the integral and functional scales are summarised in Table 5. The proportionality coefficients for the streamwise and transverse length scales are consistent for $k^{3/2}/\epsilon$ and $k^{1/2}/\left(\bar{v}_1/D_j\right)$. This indicates that the integral length scales of the random transverse velocity are relatively isotropic along the nozzle lip line. The proportionality coefficients weakly vary with Mach number, but are within the RMS dispersion error for both jet conditions and functional scales considered.

Table 6. Proportionality coefficients used in previous predictions with the BBSAN acoustic analogy of Morris and Miller [12]

	$c_{L^{(1)}}$	$c_{L^{(2)}}$
Morris and Miller (screech) [12]	3.25	0.30
Morris and Miller (no screech) [12]	3.00	0.30
Kalyan and Karabasov [24]	1.25	0.25

Previous implementations of the BBSAN acoustic analogy of Morris and Miller [12] have used a range of proportionality coefficients. The coefficient values that are based on the turbulence dissipation to model the RANS length scales are summarised in Table 6. All of the coefficients were determined by matching predictions to far-field acoustic mea-

surements for a single jet condition and observer location [12, 24]. There is considerable variation with the values in Table 5. In the study of Morris and Miller [12], the values were chosen based on the predicted spectrum at $\theta = 100°$ to a purely converging jet at $M_j = 1.50$ with total temperature ratios of 1.00 and 2.20 for the screeching and non-screeching cases, respectively. For the cross-stream length scale coefficient, $c_{L^{(2)}}$, a typical value of approximately 30% of the streamwise component is typically used [12,24,27]. Smaller length scale coefficients were used in the predictions of Kalyan and Karabsov [24] where the two-time scale formulation (Eq. (11)) is used with the turbulence dissipation scale. The studies by Morris and Miller, and Kalyan and Karabasov both suggest larger anisotropy in the length scales compared to the current PIV based coefficients presented in Table 5. While there is some agreement in the absolute value of the cross-stream length scale coefficients, further analysis is required to reconcile the discrepancies in the streamwise coefficients.

V.   RANS Modelling

A.   Flow-Field Simulations
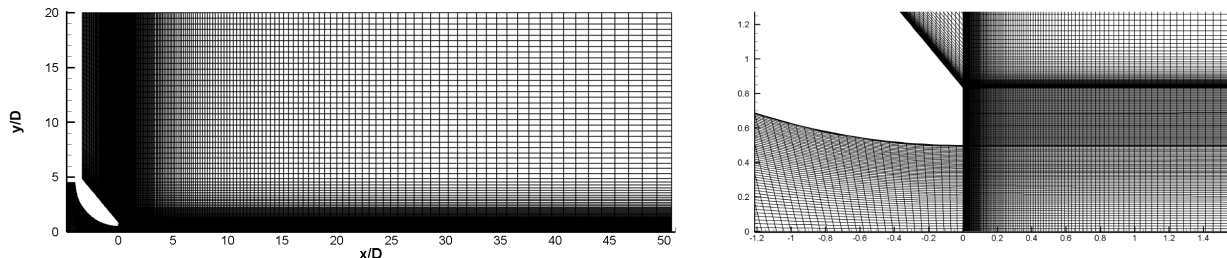
Figure 3.   Half-view computational domain with grid refinement at the nozzle exit

The LTRAC jets were numerically modelled by solving the RANS equations. A second-order density-based RANS solver was used with a $k - \omega$ SST turbulence model [50], which accounts for the adverse pressure gradients that are characteristic of supersonic flows [12, 24]. The geometry of the converging axisymmetric nozzle used in the PIV experiments was modelled by subtracting the solid sections of the nozzle from the control volume, as shown in Fig. 3. The properties of the control volume were set to the ambient air

Table 7. Summary of the RANS jet and boundary conditions

	M_j	
	1.45	1.59
NPR	3.4	4.2
D_j (mm)	16.02	16.73
Re_j ($\times 10^5$)	7.24	10.5
T_0 (K)	288	288
T_∞ (K)	288	288
P_∞ (kPa)	101.325	101.325

conditions. The boundary conditions at the nozzle inlet were set to match the experiments as temperature and pressure measurements in the near nozzle region were not available. A summary of the parameters and boundary conditions used in the RANS simulations is provided in Table 7.

The computational domain was designed to ensure boundary effects do not contaminate the solutions with axial (x) and transverse (y) dimensions of 62 and $20D$, respectively. The computational mesh had $165,571$ elements that were created using an adaptive refinement technique. The adaptive refinement technique is used to optimise the numerical simulation by reducing the computational costs and time whilst maintaining the accuracy of the results. When refining a mesh it is crucial to identify the critical zones where a refinement of the grid is needed in order to capture the physical phenomenon that is developing in these zones. As a result, only the critical zones will have fine cells, whereas in other zones where no refinement is needed, coarser cells are used. The zones where there is significant refinement are the boundary layers near the nozzle walls and the mixing layers with turbulent eddy regions (inertial range and Kolmogorov's scales). Thus, the refinement near the nozzle's exit and lip lines is required to capture the fine-scale turbulence in the mixing layer due to shear between the two flows.

The mesh refinement near the nozzle exit and in the shear layer are evident in the half-view of the computational domain. The mesh was determined by identifying and

American Institute of Aeronautics and Astronautics

subsequently refining the critical regions in the flow, such as the shear layer and shock cells that govern the BBSAN generation mechanism. The refinement was followed by several sequentially run RANS calculations to verify that the target viscous wall grid resolution was adequate ($y+ < 1$). The boundary conditions listed in Table 7 were defined at the nozzle inlet, in the free-stream, and the downstream pressure condition for the jet outflow. The ambient pressure and temperature was used to specify the far-field boundary conditions. A free-stream Mach number of 0.001 was prescribed to improve the stability of the calculations [24]. The RANS calculations were iterated until the corresponding convergence residuals of the RANS equations were less than $\sim 10^{-13}$ (round-off error) or the residuals of the various equations being solved stagnated at a level of three or more orders of magnitude less than the initial residuals.

B. Post-Processing

An inverse-distance weighted method [51] was used to interpolate the RANS solutions onto a uniformly spaced structured grid. The specific dissipation rate Ω was converted into the viscous dissipation rate ϵ according to $\epsilon = 0.09k\Omega$ [52]. The characteristic scales that inform the statistical source model were determined using the models based on the turbulence kinetic energy, dissipation rate, and eddy convection time (Table 1). The modelled RANS source sources are evaluated using the mean proportionality coefficients given in Table 5.

C. Validation

1. Mean Flow Velocity

The mean axial and transverse velocity fields that are yielded from the RANS solutions are presented with the PIV measurements in Fig. 4. The PIV and RANS fields are presented as the top and bottom halves of each contour map, respectively. The sonic line and axial locations of the shock reflection points superimposed with the outer edge of the shear layer indicated on the axial velocity contours of the PIV measurements. The axial locations of
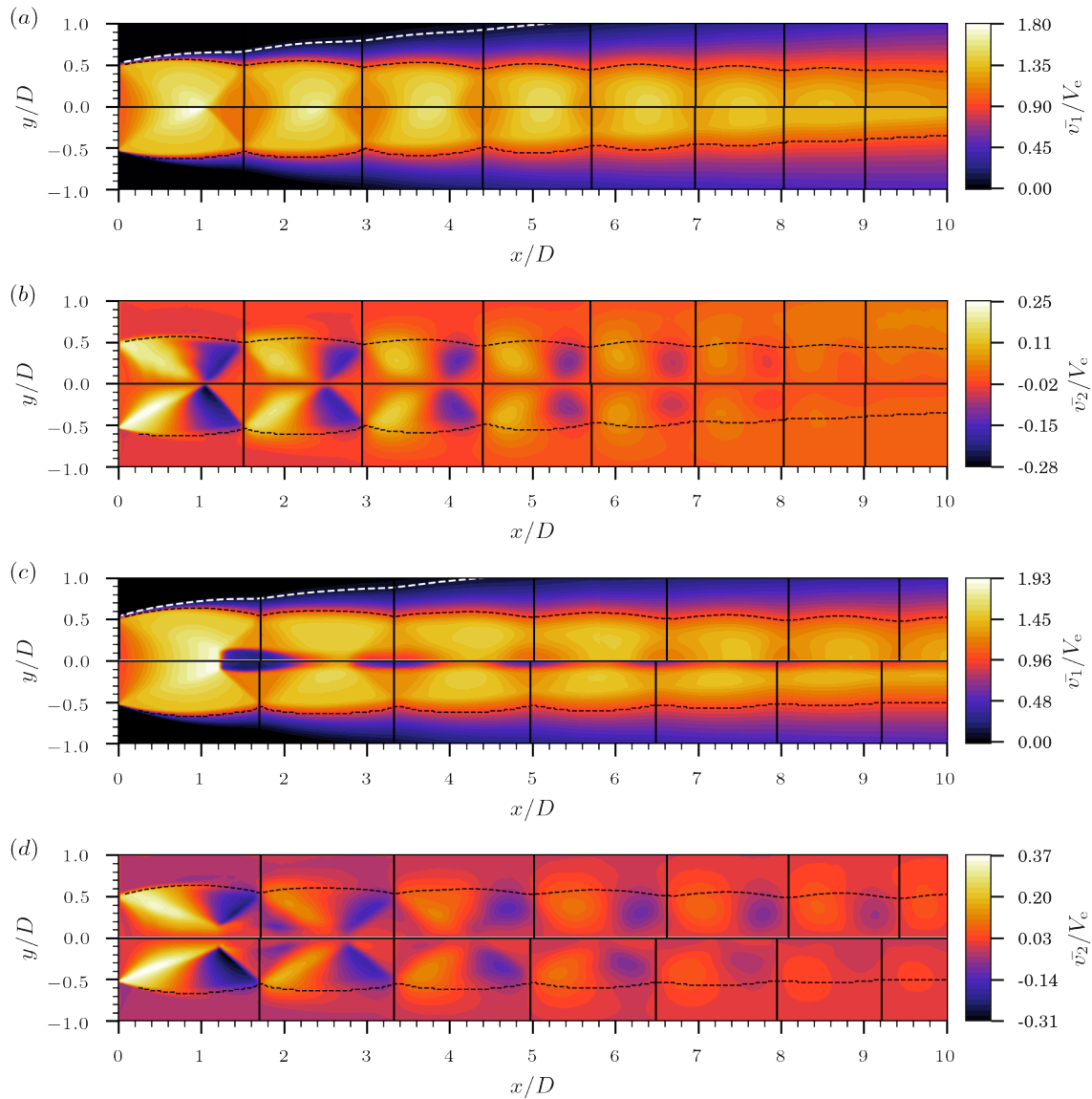
American Institute of Aeronautics and Astronautics

Figure 4. Half-plane (top: PIV; bottom: RANS) mean axial and transverse velocity fields for (a, b) $M_j =$ 1.45 **and (c, d)** 1.59.

the shock reflection points are estimated from the RANS solutions in the same way as the PIV measurements. The supersonic region is delineated by the sonic line, which is indicated by the dashed horizontal lines. The sonic line is based on the local Mach number calculated from the adiabatic total temperature given by Eq. (16).

The global flow structure is well predicted by the RANS at both Mach numbers. A quasi-periodic shock cell structure is evident in the supersonic regions of the jets. There are some discrepancies in the shock cell spacing predicted from the RANS solutions for

American Institute of Aeronautics and Astronautics
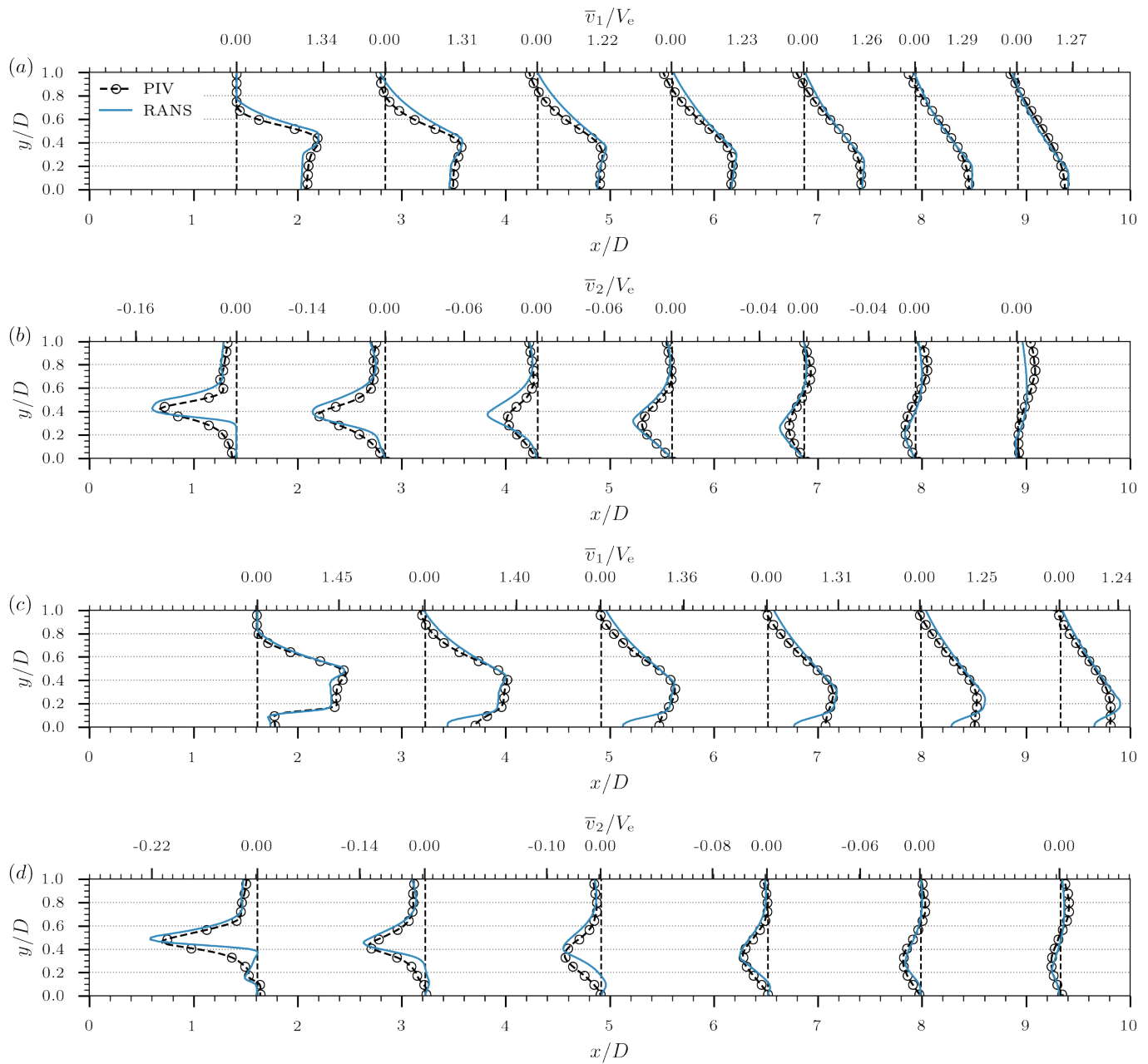
Figure 5. Axial and transverse velocity distributions near the shock reflection points for (a, b) $M_{\rm j} = 1.45$ **and (c, d)** 1.59

$M_{\rm j} = 1.59$ and $x/D > 5$. A second internal shear layer occurs for $M_{\rm j} = 1.59$ due to a Mach disk that is well resolved in both the experiments and simulations. The internal shear layer generates additional turbulence that interacts with the shocks. These interactions excite the shock cell structure, which can affect the turbulence in the outer mixing layer due to the shock motion, and probably to modulate the BBSAN. Effects from the excitation

induced by the internal shear layer turbulence are not expected to be significant in the far-field so are neglected.

Transverse distributions of the velocity flow fields are presented in Fig. 5. The distributions are extracted at the axial locations that are marked by the vertical dashed lines, which correspond to regions $0.1D$ upstream of the shock reflection points as determined from the PIV measurements (Fig. 4). There is generally good agreement between the measurements and simulations. The discrepancies in the regions adjacent to the nozzle lip line ($y/D = 0.5$) suggest that a faster shear layer growth rate is predicted by the RANS solver. The larger discrepancy for the $M_j = 1.59$ jet may be due to the complex internal shear layer structure associated with the Mach disk at $x/D \approx 1.2$. Despite these differences, there is generally good agreement between the measurements and simulations.

2. Turbulence Kinetic Energy and Dissipation Rate
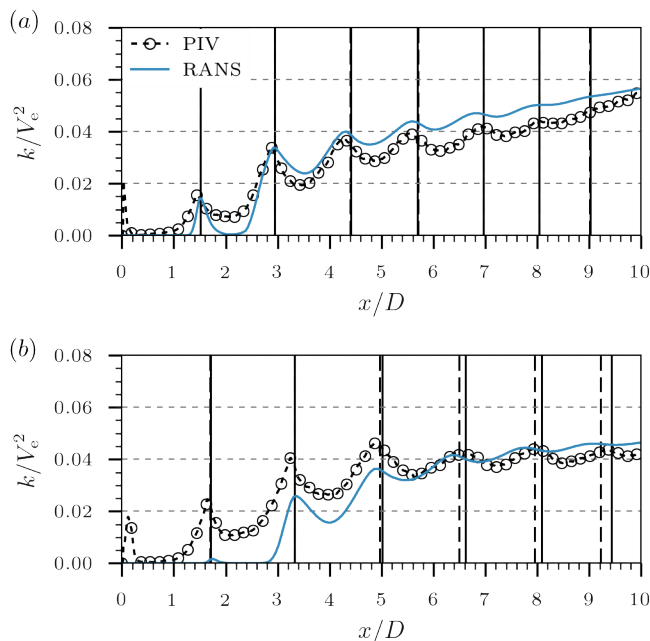
Figure 6. **Mean turbulence kinetic energy along the nozzle lip line ($y/D = 0.5$) for M_j of (a) 1.45 and (b)** 1.59

The agreement is consistent for the mean turbulence kinetic energy and dissipation that are used to calculate the functional scales. Distributions of the mean turbulence kinetic
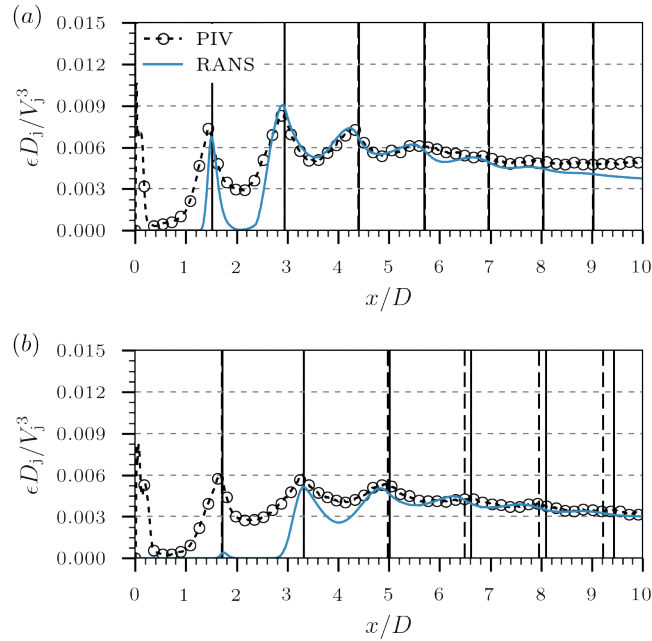
Figure 7. Mean turbulence dissipation rate along the nozzle lip line ($y/D = 0.5$) for M_j of (a) 1.45 and (b) 1.59

energy and dissipation rate along the nozzle lip line are shown in Fig.6 and 7, respectively. The shock reflection points calculated from the PIV fluctuations and RANS are indicated by the vertical solid and dashed lines, respectively. The mean turbulence statistics calculated from the random velocity fluctuations measured with PIV are included. The RANS solutions reasonably predict both the turbulence kinetic energy and dissipation rate. The limits of PIV in thin shear layers are expected to contribute to large discrepancies observed near the nozzle exit. Discrepancies between the PIV and RANS are larger for the jet at $M_j = 1.59$ from $x/D > 1.5$ where the turbulence kinetic energy and dissipation rate are underpredicted. Local maxima of the mean turbulence properties are approximately coincident with the shock reflection points.

D. Shock Pressure

The shock pressure required to reconstruct the equivalent BBSAN sources is directly available from the RANS solutions. Distributions along the nozzle lip line are shown in Fig. 8 with the shock pressure modelled from the PIV measurements using isentropic
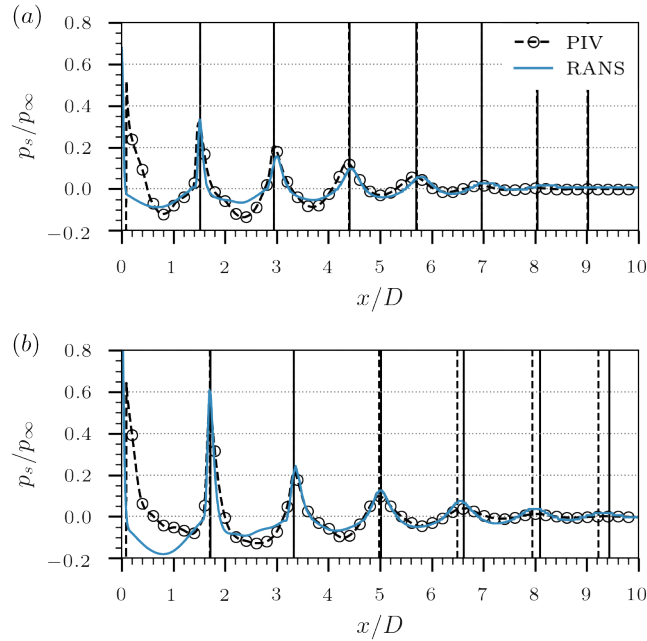
American Institute of Aeronautics and Astronautics

Figure 8. Shock pressure along the nozzle lip line ($y/D = 0.5$) for M_j of **(a)** 1.45 **and (b)** 1.59

and adiabatic flow conditions outlined in Sec. 1. The region of integration for the mean pressure gradient is marked by the horizontal dashed lines overlaid in Fig. 4. Traces of the shock pressure along the nozzle lip line normalised by the ambient pressure are shown in Fig. 8. The shock reflection points are overlaid in the same way as in Sec. 2. There is reasonable agreement in the location of the peak pressure and amplitudes over the length of the streamwise domain for both jet conditions. Discrepancies in the shock pressure distributions from the PIV and RANS data are largest before the first shock reflection point for $x/D < 1.5$. For this region, the turbulent kinetic energy is small, and thus will not contribute to the radiated sound.

E.   RANS Scales

The mean proportionality coefficient was used to model the RANS scales as the coefficients are reasonably insensitive to the operating condition. The second-order RANS length scales that define the BBSAN source correlation model given by Eq. (9) are shown in Fig. 9. The axial locations of the shock reflection points are indicated by the vertical
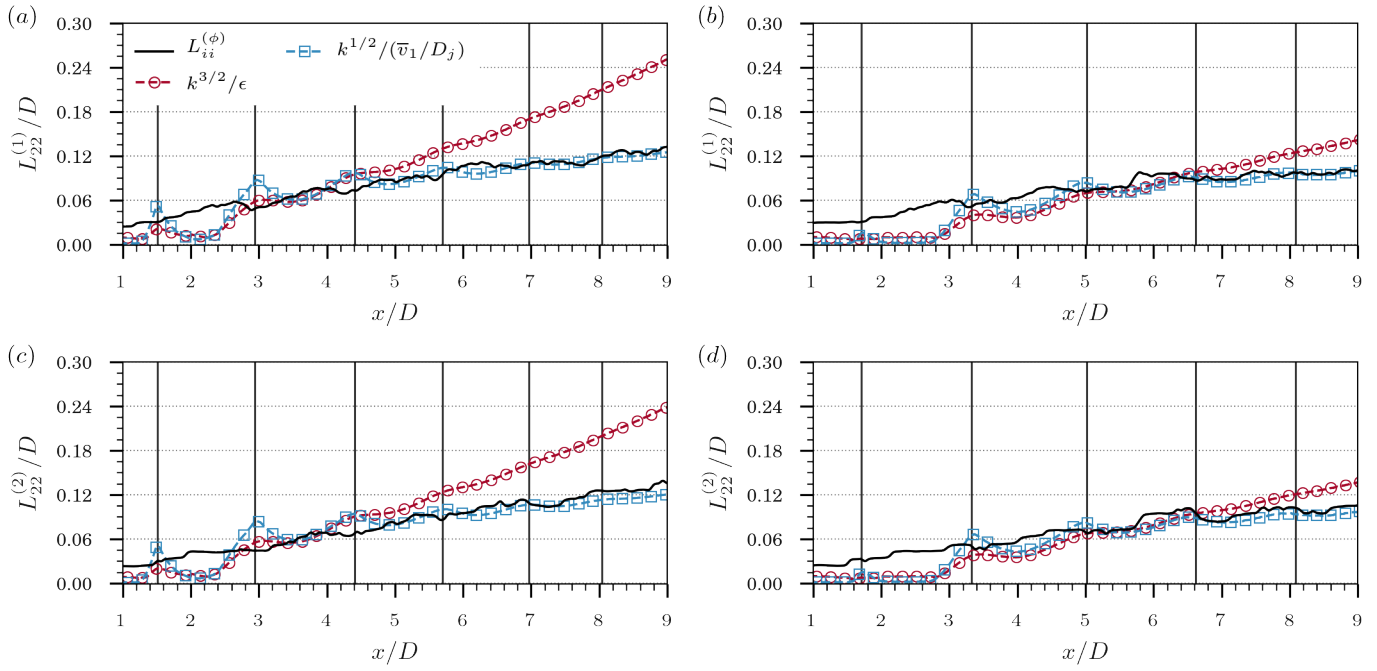
American Institute of Aeronautics and Astronautics

Figure 9. Distributions of the second-order RANS length scales along nozzle lip line ($y/D = 0.5$)

Table 8. RMSE (%) of the RANS length scales along the nozzle lip line ($y/D = 0.5$) [22]

	M_{j}	
	1.45	1.59
$k^{3/2}/\epsilon$:		
$L_{22}^{(1)}$	4.98%	4.07%
$L_{22}^{(2)}$	4.15%	3.98%
$k^{1/2}/(\bar{v}_1/D_{\mathrm{j}})$:		
$L_{22}^{(1)}$	1.67%	2.42%
$L_{22}^{(2)}$	1.97%	2.49%

lines. The integral length scales of the random velocity fluctuations extracted from the PIV measurements are indicated by the solid line, thus cannot be directly compared to those of screeching jets. The large eddy convection based scale has excellent agreement with the integral length scales for $x/D > 4$ and $x/D > 5$ for the jets at $M_{\mathrm{j}} = 1.45$ and

1.59, respectively. Both models underpredict the integral value for $x/D < 3$. This region has larger errors for $M_j = 1.59$ due to the discrepancies in the mean turbulence statistics shown in Fig. 6 and 7. In the downstream regions for $x/D > 5$, the turbulence dissipation based length scale diverges from the integral length scale for both Mach numbers.

The root meet square error (RMSE) of the RANS length scales are given in Table 8. The RMSE is expressed as a percentage of the local integral length scale value such that

$$RMSE = \frac{\sqrt{\overline{\left(L_i - \hat{L}_i\right)^2}}}{L_i}$$

The turbulence dissipation and large eddy convection based models both approximate the integral transverse velocity length scales to within 5%, which is expected to translate to a nominal error of less than 1% in the predicted BBSAN spectra [24]. The trends in the RMSE of the RANS length scales support the qualitative observations that were made directly from the distributions shown in Fig. 9.

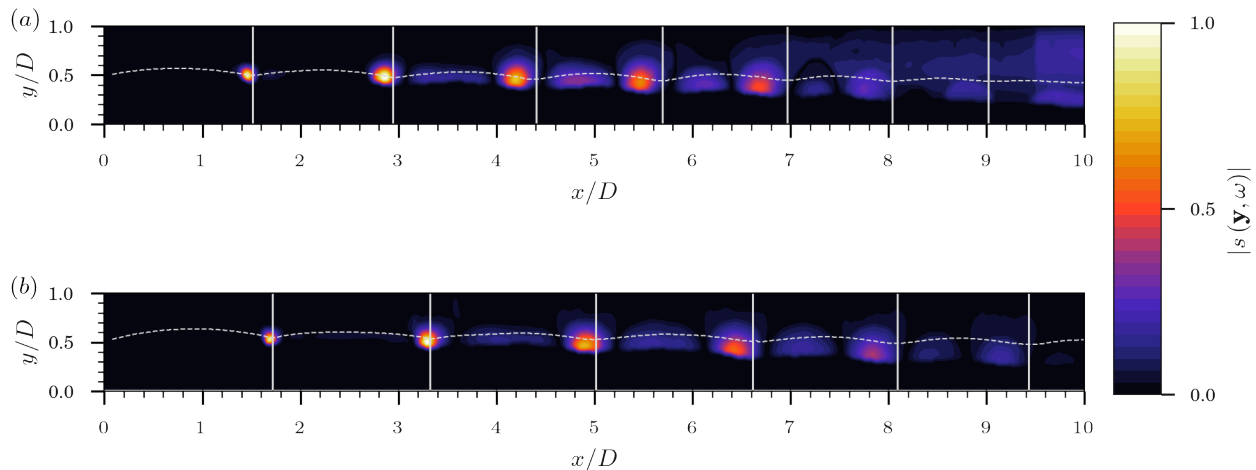## VI. BBSAN Source Reconstruction

Figure 10.   Equivalent BBSAN sources at $Sr = 1$ for (a) $M_j = 1.45$ and (b) 1.59 informed by the integral length scales

The noise sources at the peak BBSAN frequency of $Sr = 1$ for $M_j = 1.45$ and 1.59 are
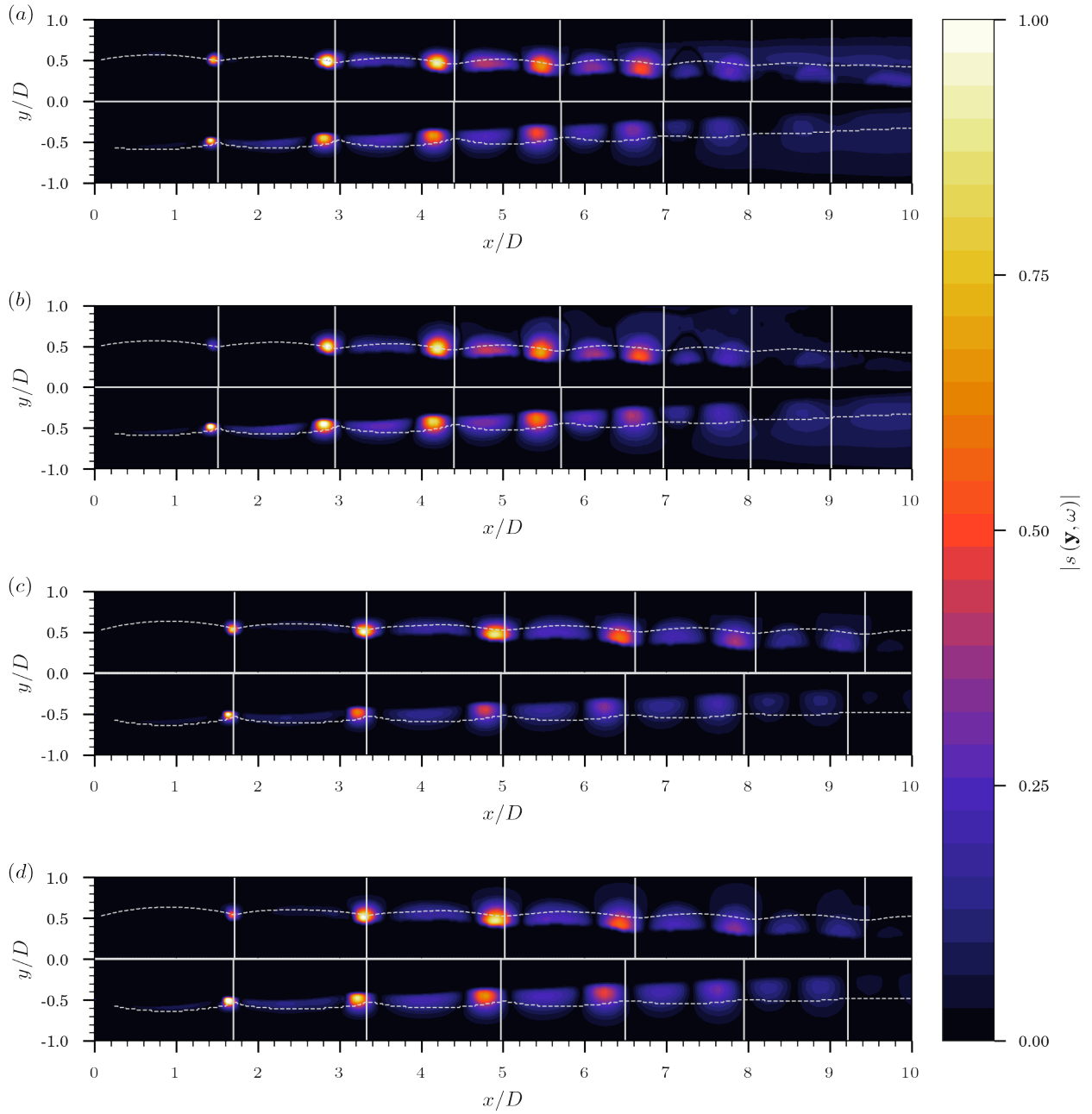
Figure 11. Equivalent BBSAN sources at $Sr = 1$ for **(a,b)** $M_j = 1.45$ **and (c,d)** 1.59 **using the two time scale formulation with (a, c)** $\tau_1 = k/\epsilon$, **and (b, d)** $D_j/\overline{V_1}$

approximated by Eq. (10). The equivalent BBSAN sources that were reconstructed using the integral length scales and the time scales given by Eq. (25) are presented in Fig. 10. The source amplitude is normalised by the peak intensity value. Regions inside the potential core are masked as the sound is not expected to contribute to the far-field acoustic PSD in
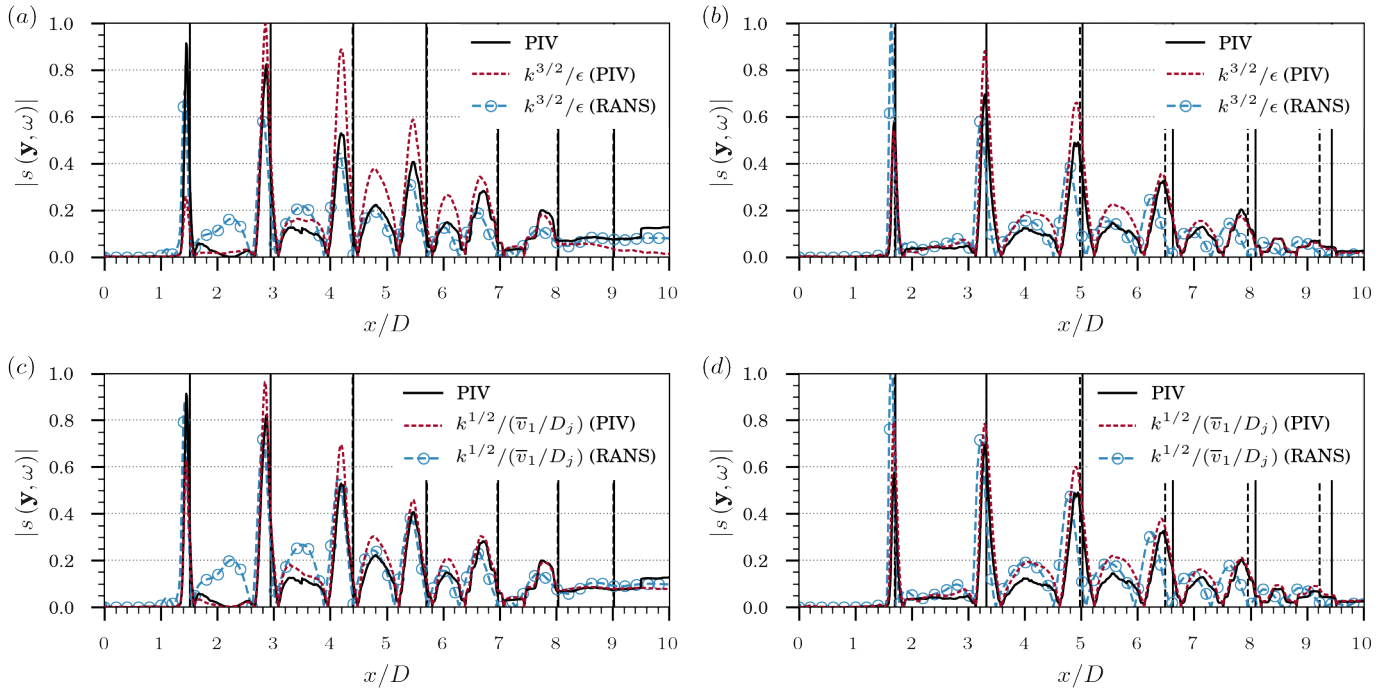
American Institute of Aeronautics and Astronautics

Figure 12. Distributions along the nozzle lip line of the BBSAN source intensity for (a,c) $M_j = 1.45$ and (b,d) 1.59

Table 9. RMSE (%) of the modelled source amplitudes along the nozzle lip line ($y/D = 0.5$)

	M_j	
	1.45	1.59
$k^{3/2}/\epsilon$		
PIV	1.44%	1.32%
RANS	1.01%	1.84%
$k^{1/2}/(\overline{v}_1/D_j)$		
PIV	0.81%	0.95%
RANS	0.51%	1.62%

the sideline direction.

The BBSAN sources approximately lie along the sonic line where shocks can interact with the large-scale turbulence in the shear layer. The regions that contribute most to the radiated BBSAN are localised upstream of the shock reflection points. The relative

regions contributing strongly to the radiation of BBSAN in relation to the shock reflection points is consistent with the literature [23, 24, 27, 53, 54]. However, the BBSAN sources are primarily observed within the first four to five shock-cells, which contradicts the studies of Norum and Seiner [55], and Seiner and Yu [56] where the BBSAN sources are located towards the end of the potential core. Discrepancies in the absolute position of the equivalent BBSAN sources are consistent with the observations of Miller [27], who notes that refraction effects of the shear layer that are not accounted for in the aforementioned studies result in the sources appearing multiple diameters downstream from their actual location. Additionally, Norum and Seiner, and Seiner and Yu considered nozzles with tabs protruding into the jet flow to suppress screech, which has been shown to modify the overall flow structure [57].

As the turbulence kinetic energy increases, the regions where there are strong correlations associated with the production of BBSAN spread out in the transverse directions. The BBSAN sources located directly upstream of the shock reflection points alternate with regions of weaker intensity. These regions of weaker intensity are initially elongated in the streamwise direction before becoming more isotropic as the shear layers begin to develop fully.

Similar features are observed in the equivalent BBSAN sources that were modelled using the local turbulence scales. The modelled BBSAN sources are presented in Fig.11 at the peak BBSAN frequency of $Sr = 1$ with the top and bottom halves of each contour map corresponding to the sources extracted from the PIV and RANS, respectively, with the shock reflection points and sonic line marked. There is excellent agreement between the modelled PIV and RANS source amplitude maps. The modelled sources are concentrated upstream of the shock reflection points, which is consistent with the BBSAN sources calculated using the integral length scales.

The source distributions in Fig. 12 highlight discrepancies in the amplitude. The shock reflection points determined from the PIV measurements and RANS solutions are indicated by the vertical and dashed lines, respectively. The discrepancies are generally

American Institute of Aeronautics and Astronautics

largest in local peaks that are observed directly up- and downstream of the shock reflection points. The discrepancies for the $M_j = 1.59$ jet are exacerbated by differences in the shock cell spacing predicted in the RANS solutions. However, there is reasonable agreement between the source amplitudes relative to the axial location of the shock reflections points. These regions also correspond to where the turbulence scales overpredict the integral length scales, as can be seen in Fig. 9. The agreement between the integral scales and the large eddy convection scale is improved for $x/D > 3$, which also corresponds to more reliable estimates of the source amplitude distributions shown in Fig. 12. The predicted source amplitudes that were modelled using the turbulence dissipation based RANS scales are not greatly affected by the overestimation of the integral length scales shown in Fig. 9.

The RMSE of the BBSAN source distributions along the nozzle lip line are shown in Table 9. The error is calculated relative to the distributions of the BBSAN sources shown in Fig. 10, which are based on the integral length scales. The RMSE of the sources modelled from the PIV measurements are similar at both jet conditions, with a mean error of 1.33% and 0.86% for $k^{3/2}/\epsilon$ and $k^{1/2}/\left(\overline{v}_1/D_j\right)$, respectively. The error of the modelled RANS noise sources for $M_j = 1.45$ is smaller than for the sources constructed using the equivalent scale extracted from the PIV measurements. The smallest error for all cases is obtained with the large eddy convection based scale, $D_j/\overline{V_1}$, which is not usually considered for noise modelling applications.

VII.   Conclusions

BBSAN radiated by screeching underexpanded unheated round jets was studied at the root source level. The BBSAN sources were considered within the context of an acoustic analogy. The acoustic analogy was informed by high spatial resolution 2D-2C PIV measurements and RANS solutions. The RANS scales were determined using proportionality coefficients based on linear fits of the local turbulence scales extracted from the PIV measurements to the integral scales of the random velocity fluctuations. The proportionality coefficients were shown to be insensitive to the operating condition of the jet. The RANS

length scales based on $k^{3/2}/\epsilon$ and $k^{1/2}/(\overline{v_1}/D_j)$ were shown to model the integral scales within 3% for $1 < x/D < 9$ at both jet conditions.

The equivalent BBSAN sources at the peak BBSAN frequency of $Sr = 1$ were reconstructed. The equivalent BBSAN sources were shown to be distributed along the sonic line with localised regions of high source intensity directly upstream of the shock reflection points. These regions alternated with regions of weaker intensity that were overestimated when the local turbulence scales were used in the reconstruction. The equivalent BBSAN source distribution along the nozzle lip line was modelled to within 2% of the local value for all scales and conditions. The smallest errors were achieved when the large eddy convection based scale $k^{1/2}/(\overline{v_1}/D_j)$ is used, which was shown to most accurately model the integral length scales for both the PIV and the RANS. The latter is recommended as a replacement for the standard turbulence dissipation scale in low-order BBSAN models.

Acknowledgments

References

[1] Powell, A., "On the mechanism of choked jet noise," *Proceedings of the Physical Society. Section B*, Vol. 66, No. 12, 1953, pp. 1039. doi:10.1088/0370-1301/66/12/306.

[2] Krothapalli, A., Hsia, Y., Baganoff, D., and Karamcheti, K., "The role of screech tones in mixing of an underexpanded rectangular jet," *Journal of Sound and Vibration*, Vol. 106, No. 1, 1986, pp. 119–143. doi:10.1016/S0022-460X(86)80177-8.

[3] Seiner, J. and Norum, T., "Experiments of shock associated noise of supersonic jets," *12th Fluid and Plasma Dynamics Conference*, 1979, p. 1526. doi:10.2514/6.1979-1526.

[4] Norum, T. D. and Seiner, J. M., "Broadband shock noise from supersonic jets," *AIAA journal*, Vol. 20, No. 1, 1982, pp. 68–73. doi:10.2514/3.51048.

[5] Tam, C. K. W., "Stochastic model theory of broadband shock associated noise from supersonic jets," *Journal of Sound and Vibration*, Vol. 116, No. 2, 1987, pp. 265–302. doi:10.1016/S0022-460X(87)81303-2.

American Institute of Aeronautics and Astronautics

[6] Viswanathan, K., Alkislar, M., and Czech, M., "Characteristics of the shock noise component of jet noise," *AIAA journal*, Vol. 48, No. 1, 2010, pp. 25. doi:10.2514/1.38521.

[7] Arroyo, C. P., Daviller, G., Puigt, G., Airiau, C., and Moreau, S., "Identification of temporal and spatial signatures of broadband shock-associated noise," *Shock Waves*, 2018, pp. 1–18. doi:10.1007/s00193-018-0806-4.

[8] Harper-Bourne, M. and Fisher, M. J., "The noise from shock waves in supersonic jets," *AGARD Noise Mech. 13 p(SEE N 74-22640 14-02)*, 1974.

[9] Tam, C. K. and Chen, K., "A statistical model of turbulence in two-dimensional mixing layers," *Journal of Fluid Mechanics*, Vol. 92, No. 2, 1979, pp. 303–326. doi:10.1017/S002211207900063X.

[10] Tam, C. K. W., Jackson, J. A., and Seiner, J. M., "A multiple-scales model of the shock-cell structure of imperfectly expanded supersonic jets," *Journal of Fluid Mechanics*, Vol. 153, 1985, pp. 123–149. doi:10.1017/S0022112085001173.

[11] Tam, C. K. W., "Broadband shock-associated noise of moderately imperfectly expanded supersonic jets," *Journal of Sound and Vibration*, Vol. 140, No. 1, 1990, pp. 55–71. doi:10.1016/0022-460X(90)90906-G.

[12] Morris, P. J. and Miller, S. A. E., "Prediction of broadband shock-associated noise using Reynolds-averaged Navier-Stokes computational fluid dynamics," *AIAA journal*, Vol. 48, No. 12, 2010, pp. 2931–2944. doi:10.2514/1.J050560.

[13] Lighthill, M. J., "On sound generated aerodynamically. I. General theory," *Proceedings of the Royal Society of London A: Mathematical, Physical and Engineering Sciences*, Vol. 211, The Royal Society, 1952, pp. 564–587. doi:10.1098/rspa.1952.0060.

[14] Lyrintzis, A. S., "Surface integral methods in computational aeroacoustics—From the (CFD) near-field to the (Acoustic) far-field," *International journal of aeroacoustics*, Vol. 2, No. 2, 2003, pp. 95–128. doi:10.1260/147547203322775498.

[15] Lyrintzis, A. S., "The use of Kirchhoff's method in computational aeroacoustics," *Journal of Fluids Engineering*, Vol. 116, No. 4, 1994, pp. 665–676. doi:10.1115/1.2911834.

[16] Williams, J. E. F. and Hawkings, D. L., "Sound generation by turbulence and surfaces in arbitrary motion," *Philosophical Transactions of the Royal Society of London A: Mathematical, Physical and Engineering Sciences*, Vol. 264, No. 1151, 1969, pp. 321–342. doi:10.1098/rsta.1969.0031.

[17] Viswanathan, K. and Sankar, L., "Toward the direct calculation of noise: fluid/acoustic coupled simulation," *AIAA journal*, Vol. 33, No. 12, 1995. doi:10.2514/3.12979.

[18] Morris, P. J. and Farassat, F., "Acoustic analogy and alternative theories for jet noise prediction," *AIAA journal*, Vol. 40, No. 4, 2002, pp. 671–680. doi:10.2514/2.1699.

[19] Morris, P. J. and Zaman, K. B. M. Q., "Velocity measurements in jets with application to noise source modeling," *Journal of sound and vibration*, Vol. 329, No. 4, 2010, pp. 394–414. doi:10.1016/j.jsv.2009.09.024.

[20] Morris, P. and Zaman, K., "Two component velocity correlations in jets and noise source modeling," *16th AIAA/CEAS Aeroacoustics Conference*, 2010, p. 3781. doi:10.2514/6.2010-3781.

[21] Tan, D. J., Soria, J., Honnery, D., and Edgington-Mitchell, D., "Novel Method for Investigating Broadband Velocity Fluctuations in Axisymmetric Screeching Jets," *AIAA Journal*, 2017. doi:10.2514/1.J055606.

American Institute of Aeronautics and Astronautics

[22] Tan, D. J., Honnery, D., Kalyan, A., Gryazev, V., Karabasov, S., and Edgington-Mitchell, D., "Correlation Analysis of High Resolution Particle Image Velocimetry Data of Screeching Jets (*under review*)," *AIAA journal*, 2018.

[23] Savarese, A., Jordan, P., Girard, S., Collin, E., Porta, M., and Gervais, Y., "Experimental study of shock-cell noise in underexpanded supersonic jets," *19th AIAA/CEAS Aeroacoustics Conference*, 2013, p. 2080. doi:10.2514/6.2013-2080.

[24] Kalyan, A. and Karabasov, S. A., "Broadband shock associated noise predictions in axisymmetric and asymmetric jets using an improved turbulence scale model," *Journal of Sound and Vibration*, Vol. 394, 2017, pp. 392–417. doi:10.1016/j.jsv.2017.01.027.

[25] Ray, P. K. and Lele, S. K., "Sound generated by instability wave/shock-cell interaction in supersonic jets," *Journal of fluid mechanics*, Vol. 587, 2007, pp. 173–215. doi:10.1017/S0022112007007306.

[26] Proudman, I., "The generation of noise by isotropic turbulence," *Proceedings of the Royal Society of London A: Mathematical, Physical and Engineering Sciences*, Vol. 214, The Royal Society, 1952, pp. 119–132. doi:10.1098/rspa.1952.0154.

[27] Miller, S. A., "The scaling of broadband shock-associated noise with increasing temperature," *International Journal of Aeroacoustics*, Vol. 14, No. 1-2, 2015, pp. 305–326. doi:10.1260/1475-472X.14.1-2.305.

[28] Ribner, H. S., "Quadrupole correlations governing the pattern of jet noise," *Journal of Fluid Mechanics*, Vol. 38, No. 01, 1969, pp. 1–24. doi:10.1017/S0022112069000012.

[29] Bridges, J. E. and Wernet, M. P., "Measurements of Turbulent Convection Speeds in Multistream Jets Using Time-Resolved PIV," *23rd AIAA/CEAS Aeroacoustics Conference*, 2017, p. 4041. doi:10.2514/6.2017-4041.

[30] Batchelor, G. K., *The theory of homogeneous turbulence*, Cambridge university press, 1953. doi:10.1002/qj.49707934126.

[31] Hunt, J., Moin, P., Lee, M., Moser, R., Spalart, P., Mansour, N., Kaimal, J., and Gaynor, E., "Cross correlation and length scales in turbulent flows near surfaces," *Advances in Turbulence 2*, Springer, 1989, pp. 128–134. doi:10.1007/978-3-642-83822-4.

[32] Bailly, C., Lafon, P., Sé, and Candel, b., "Subsonic and supersonic jet noise predictions from statistical source models," *AIAA journal*, Vol. 35, No. 11, 1997, pp. 1688–1696. doi:10.2514/2.33.

[33] Edgington-Mitchell, D. M., Oberleithner, K., Honnery, D. R., and Soria, J., "Coherent structure and sound production in the helical mode of a screeching axisymmetric jet," *Journal of Fluid Mechanics*, Vol. 748, 2014, pp. 822–847. doi:10.1017/jfm.2014.173.

[34] Edgington-Mitchell, D. M., Honnery, D. R., and Soria, J., "The underexpanded jet Mach disk and its associated shear layer," *Physics of Fluids (1994-present)*, Vol. 26, No. 9, 2014, pp. 096–101. doi:10.1063/1.4894741.

[35] Soria, J., "An investigation of the near wake of a circular cylinder using a video-based digital cross-correlation particle image velocimetry technique," *Experimental Thermal and Fluid Science*, Vol. 12, No. 2, 1996, pp. 221–233. doi:10.1016/0894-1777(95)00086-0.

[36] Mitchell, D. M., Honnery, D. R., and Soria, J., "Near-field structure of underexpanded elliptic jets," *Experiments in fluids*, Vol. 54, No. 7, 2013, pp. 1–13. doi:10.1007/s00348-013-1578-3.

[37] Mitchell, D. M., Honnery, D. R., and Soria, J., "Particle relaxation and its influence on the particle image velocimetry cross-correlation function," *Experiments in fluids*, Vol. 51, No. 4, 2011, pp. 933–947. doi:10.1007/s00348-011-1116-0.

[38] Agüí, J. C. and Jimenez, J., "On the performance of particle tracking," *Journal of fluid mechanics*, Vol. 185, 1987, pp. 447–468. doi:10.1017/S0022112087003252.

[39] Dash, S. M., Wolf, D. E., and Seiner, J., "Analysis of turbulent underexpanded jets. I-Parabolized Navier-Stokes model, SCIPVIS," *AIAA journal*, Vol. 23, No. 4, 1985, pp. 505–514. doi:10.2514/3.8944.

[40] van Oudheusden, B. W., Scarano, F., Roosenboom, E. W., Casimiri, E. W., and Souverein, L. J., "Evaluation of integral forces and pressure fields from planar velocimetry data for incompressible and compressible flows," *Experiments in Fluids*, Vol. 43, No. 2-3, 2007, pp. 153–162.

[41] Hall, K. C., Thomas, J. P., and Dowell, E. H., "Proper orthogonal decomposition technique for transonic unsteady aerodynamic flows," *AIAA journal*, Vol. 38, No. 10, 2000, pp. 1853–1862. doi:10.2514/2.867.

[42] Morris, P., "Broadband jet noise amplification by a pure tone excitation," *NASA Technical Reports*, Vol. 163269, 1980.

[43] Ahuja, K. K., Lepicovsky, J., Tam, C. K. W., Morris, P. J., and Burrin, R. H., "Tone-excited jet: Theory and experiments," *NASA Technical Reports*, 1982.

[44] Fleury, V., Bailly, C., Jondeau, E., Michard, M., and Juvé, D., "Space-time correlations in two subsonic jets using dual particle image velocimetry measurements," *AIAA journal*, Vol. 46, No. 10, 2008, pp. 2498–2509. doi:10.2514/1.35561.

[45] André, B., Castelain, T., and Bailly, C., "Investigation of the mixing layer of underexpanded supersonic jets by particle image velocimetry," *International Journal of Heat and Fluid Flow*, Vol. 50, 2014, pp. 188–200. doi:10.1016/j.ijheatfluidflow.2014.08.004.

[46] Glauser, M. N. and George, W. K., "Application of multipoint measurements for flow characterization," *Experimental Thermal and Fluid Science*, Vol. 5, No. 5, 1992, pp. 617–632. doi:10.1016/0894-1777(92)90018-Z.

[47] Tinney, C. E., Glauser, M. N., and Ukeiley, L. S., "Low-dimensional characteristics of a transonic jet. Part 1. Proper orthogonal decomposition," *Journal of Fluid Mechanics*, Vol. 612, 2008, pp. 107–141. doi:10.1017/S0022112008002978.

[48] Tinney, C. E., "Proper grid resolutions for the proper basis." *AIAA 47th Aerospace Sciences Meeting and Exhibit, Orlando, Florida, USA, AIAA paper*, Vol. 68, 2009. doi:10.2514/6.2009-68.

[49] Atkinson, C., Buchmann, N. A., Amili, O., and Soria, J., "On the appropriate filtering of PIV measurements of turbulent shear flows," *Experiments in fluids*, Vol. 55, No. 1, 2014, pp. 1654. doi:10.1007/s00348-013-1654-8.

[50] Menter, F. R. et al., "Two-equation eddy-viscosity turbulence models for engineering applications," *AIAA journal*, Vol. 32, No. 8, 1994, pp. 1598–1605. doi:10.2514/3.12149.

[51] Łukaszyk, S., "A new concept of probability metric and its applications in approximation of scattered data sets," *Computational Mechanics*, Vol. 33, No. 4, 2004, pp. 299–304. doi:10.1007/s00466-003-0532-2.

American Institute of Aeronautics and Astronautics

[52] Wilcox, D. C., *Turbulence Modeling for CFD (Third Edition)*, D C W Industries, 2006.

[53] Norum, T. and Seiner, J., "Location and propagation of shock associated noise from supersonic jets," *6th Aeroacoustics Conference*, 1980, p. 983. doi:10.2514/6.1979-1526.

[54] Bridges, J. and Wernet, M. P., "Turbulence associated with broadband shock noise in hot jets," *14th AIAA/CEAS Aeroacoustics Conference (29th AIAA Aeroacoustics Conference)*, 2008, p. 2834. doi:10.2514/6.2008-2834.

[55] Norum, T. D. and Seiner, J. M., "Measurements of mean static pressure and far field acoustics of shock containing supersonic jets," *NASA Technical Reports*, Vol. 84521, 1982.

[56] Seiner, J. and Yu, J. C., "Acoustic near-field properties associated with broadband shock noise," *AIAA journal*, Vol. 22, No. 9, 1984, pp. 1207–1215. doi:10.2514/3.8762.

[57] André, B., Castelain, T., and Bailly, C., "Effect of a tab on the aerodynamical development and noise of an underexpanded supersonic jet," *Comptes Rendus Mécanique*, Vol. 341, No. 9-10, 2013, pp. 659–666.

American Institute of Aeronautics and Astronautics